Received: 15 June 2016 | Revised: 1 June 2017 | Accepted: 2 September 2017

DOI: 10.1002/cnm.2925

RESEARCH ARTICLE - FUNDAMENTAL

WILEY

Relative pressure estimation from velocity measurements in blood flows: State-of-the-art and new approaches

Cristóbal Bertoglio[1,2] | Rodolfo Nuñez[1] | Felipe Galarce[1,3] | David Nordsletten[4] | Axel Osses[1]

[1]Center for Mathematical Modeling, Universidad de Chile, Santiago, Chile

[2]Johann Bernoulli Institute, University of Groningen, Groningen, The Netherlands

[3]Civil Engineering School, Pontificia Universidad Católica de Valparaiso, Valparaiso, Chile

[4]Department of Biomedical Engineering, King's College of London, London, UK

Correspondence
Cristóbal Bertoglio, Johann Bernoulli Institute, University of Groningen, Nijenborgh 9, 9747 AG Groningen, The Netherlands.
Email: c.a.bertoglio@rug.nl

Funding information
BHF New Horizons, Grant/Award Number: NH/11/5/29058; Engineering and Physical Sciences Research Council, Grant/Award Number: EP/N011554/1

Abstract

The relative pressure difference across stenotic blood vessels serves as an important clinical index for the diagnosis of many cardiovascular diseases. While the clinical gold standard for relative pressure difference measurements is invasive catheterization, Phase-Contrast Magnetic Resonance Imaging has emerged as a promising tool for enabling a noninvasive quantification, by linking highly spatially resolved velocity measurements with relative pressures via the incompressible Navier-Stokes equations. In this work, we provide a review and analysis of current methods for relative pressure estimation and propose 3 additional techniques. Methods are compared using synthetic data from numerical examples, and sensitivity to subsampling and noise was explored. Through our analysis, we verify that the newly proposed approaches are more robust with respect to spatial subsampling and less sensitive to noise and therefore provide improved means for estimating relative pressure differences noninvasively.

KEYWORDS

blood flows, Navier-Stokes equations, phase-contrast MRI, relative pressure estimation

1 | INTRODUCTION

The relative pressure difference (RPD) across a stenotic blood vessel is a standard clinical index that serves to assess the severity of the pathology and is used to stratify patients for therapy. Examples include the use of RPD in aortic coarctation patients,[1] valve stenosis,[2,3] and congenital heart diseases.[4] The current gold standard procedure for measuring RPD in clinical practice is through invasive X-ray–guided pressure catheterization; however, because of its invasiveness, alternative techniques, such as doppler echocardiography, are often used.[5]

Phase-Contrast Magnetic Resonance Imaging (PCMRI)[6] allows velocity measurements of blood flows, noninvasively and temporally resolved at selected planes (2D) or in the whole thorax (3D, or sometimes also called *4D-Flow*). While RPD is most often evaluated clinically using doppler echocardiography, 3D-PCMRI is gaining increasing popularity since it permits quantification of complex blood flow patterns in large vessels and the heart.[7] Moreover, recent work has demonstrated that incorporating the spatial variation not typically observed in standard echo images can have a significant impact on the pressure estimates.[8] 3D-PCMRI allows measurement of the velocity field with spatial and temporal resolutions typically ranging from 1.5 to 3 mm^3 and 20 to 40 ms, respectively, and noise levels of around 15% of the maximal velocity.[9]

Previous works have presented methods to estimate RPD from the PCMRI-measured velocities and the Navier-Stokes equations (NSE). We can classify the methods into 3 types depending on their computational complexity:

- **PDE-constrained optimization methods.** When the 3D geometry of the vessel is also acquired, 2D-PCMRI measurements can be used for estimating the parameters of the boundary conditions of NSE simulations.[10-15] Naturally, 3D-PCMRI can be also used for this purpose. However, the estimated velocity and pressure fields come at the price of solving several times the NSE problem within an optimization loop.
- **State estimators**. Instead of optimizing model parameters from the measurements, the data assimilation problem can be written as a balance between a model-measurement misfit and the residual of the mathematical model. Then, by minimizing with respect to the velocity field itself, a modified NSE appears, which includes a feedback term proportional to the difference between the measured and compute velocities.[16-18] While these approaches are effective for coping with uncertainties in the initial condition, they do not allow to estimate parameters. If both initial condition and parameters have to be jointly estimated, a fully sequential data assimilation approach is the method of choice, see, eg, Moireau et al,[19] for examples in hemodynamics. Sequential data assimilation allows however to obtain an estimation of the pressure and velocity fields at the cost of only one forward simulation of the NSE, as far enough computational capabilities are available.
- **Direct estimation methods**. These methods are defined only from 3D data and are based on directly inserting the measured velocity field into the NSE and therefore solving for the pressure field only while no estimate for the velocity is obtained apart from the measured one. To date, 3 variants have been proposed in the literature.[20-22] These approaches have the important practical advantage that the computational cost is enormously reduced with respect to the partial differential equation (PDE)–constrained optimization and the observer-based approaches and therefore has been already used in the clinical context.[8,23] Direct estimation techniques also frequently avoid uncertainties encountered with state estimator and PDE-constrained optimization methods, in particular the appropriate hemodynamic boundary conditions required.

In this work, we focus on the study of the direct estimation approaches. While, among the 3 families of techniques, direct estimation approaches depend most heavily on data quality; they also provide a number of advantages. Given their implicit use of the data to estimate RPD, direct estimation approaches tend to have a low computational cost (they are all of the order of a linear mixed problem solution, Laplace solution or direct integration of the data) making them straightforward to run on standard computers. Additionally, this reduced computational cost makes these approaches more straightforward to integrate into clinical workflows that often require rapid diagnostic information.

One of the earliest direct estimation methods developed for RPD is the simplified Bernoulli estimate, which remains the most ubiquitous in clinic. This technique benefits from its limited requirements for input data, but its oversimplification of the underlying physics impacts the final accuracy of the method. One of the first techniques capable of estimating RPD from full-field data is the so-called Pressure Poisson Estimator (PPE), see, for example, previous studies.[20,24,25] It consists in directly plugging the velocity measurements into the NSE and solving a Poisson equation for the pressure.

Very recently, 2 new approaches have been published reporting better performances compared with the PPE. In Švihlová et al,[21] it was proposed to perturb the Navier-Stokes residual with an auxiliary divergence-free vector, resulting in a mixed problem for this vector and the pressure to be estimated. Therefore, it was denoted as Stokes Estimator (STE). Their tests show that the STE outperforms the PPE in terms of precision. Then in Donati et al,[22] a method was proposed, which computes the pressure drop directly from the classical integral energy balance of the incompressible NSE. Therefore, it was denoted as Work-Energy Relative Pressure (WERP) estimator. In the WERP, no numerical solution of any PDE is required (as it is the case in the PPE or STE) while only computations of integrals are needed, hence being considerable more efficient computationally than the STE and the PPE. However, the authors indicated that the method is inaccurate for small inflow/outflow, and it cannot be applied in geometries with multiple inlet and outlet. While the WERP was reported also to be more accurate than the PPE for peak flows, the STE and WERP have not been yet compared to each other.

The purpose of this manuscript is then threefold. First, to compare the methods recently proposed (STE and WERP). Secondly, to propose improvements of such methods. Thirdly, we also derive formulae of the statistical bias of all methods that, to the best of the authors knowledge, have not yet been reported. Our manuscript presents comparisons between the recently reported approaches and proposes the best candidates for relative pressure estimators, showing that some of the methods introduced here are the most accurate. Moreover, the formulae for the statistical bias allow us to explain the misleading behavior of the WERP technique and verify that all other methods have a negligible bias.

The rest of this paper is organized as follows. In Section 2, we set up the RPD estimation problem. In Section 3, we revisit the state-of-the-art methods mentioned above. In Section 4, we propose new RPD estimation approaches. In Section

5, we perform a theoretical bias analysis for all methods. In Section 6, we test and compare them using synthetic data, including sensitivity to noise, spatial, and temporal subsampling. Finally in Section 7, we discuss the results and draw some conclusions and perspectives.

2 | THE RELATIVE PRESSURE ESTIMATION PROBLEM

Let us consider an incompressible, Newtonian fluid in a bounded domain $\Omega \subset \mathbb{R}^d$, $d = 3$, modeled by the incompressible NSE[26] with the velocity $\boldsymbol{u}(t) : \Omega \to \mathbb{R}^d$ and the pressure $p(t) : \Omega \to \mathbb{R}$, $t \in [0, T]$:

$$\begin{cases} \rho \partial_t \boldsymbol{u} + \rho(\boldsymbol{u} \cdot \boldsymbol{\nabla})\boldsymbol{u} - \mu \Delta \boldsymbol{u} + \boldsymbol{\nabla} p = \boldsymbol{0} & \text{in} \quad \Omega \times [0, T], \\ \boldsymbol{\nabla} \cdot \boldsymbol{u} = 0 & \text{in} \quad \Omega \times [0, T], \end{cases} \tag{1}$$

where ρ is the density and μ the dynamic viscosity. For our purposes, Ω will be the domain around the stenosis. We also assume that the boundary of Ω is given by $\partial\Omega := \Gamma = \Gamma_i \cup \Gamma_o \cup \Gamma_w$, with $\Gamma_i \cap \Gamma_o = \emptyset$. Γ_i is the inlet boundary (ie, upstream of the obstruction), Γ_o is the outlet boundary (downstream of the obstruction), and Γ_w is the arterial wall boundary, see example in Figure 1. We define the task of the relative pressure estimation as computing the quantity:

$$\delta p = \frac{1}{|\Gamma_i|} \int_{\Gamma_i} p - \frac{1}{|\Gamma_o|} \int_{\Gamma_o} p \tag{2}$$

given (perturbed) measurements of $\boldsymbol{u}$ in Ω.

As is obtained in 3D-PCMRI (cf Section 1), we will assume that the velocity measurements are available at h-spaced discrete points of the domain Ω. Then we will build a mesh $\mathcal{T}_h$ of the domain Ω using the measurement locations, so that the measured velocity data can be interpolated to every point of Ω using simple linear piecewise finite element basis functions.

Additionally, we will assume that these space-discrete measurements will be available at N discrete measurement times $t^1, \dots, t^N$ at a constant time interval τ. We will denote the measurements as $\boldsymbol{u}_m^1, \dots, \boldsymbol{u}_m^N \in [\mathcal{P}_{1,h}]^d$, with $\mathcal{P}_{1,h}$ the usual piecewise continuous linear polynomial finite element space.

Moreover, for further analysis, we assume that the measurements include a random, additive perturbation with respect to the ground truth velocity, ie, $\boldsymbol{u}_m^n = \boldsymbol{u}_h^n + \boldsymbol{\epsilon}^n$, with $\boldsymbol{u}_h^n \in [\mathcal{P}_{1,h}]^d$ a spatial subsampling of the true field $\boldsymbol{u}$ into $[\mathcal{P}_{1,h}]^d$ at observation time t^n, and $\boldsymbol{\epsilon}^n \in [\mathcal{P}_{1,h}]^d$ a discrete noise field, with all degrees-of-freedom independently identically distributed (iid) following a normal distribution $\mathcal{N}(0, \sigma^2)$.

Notice that we assume only the reference field $\boldsymbol{u}$ to satisfy Problem (1) (in practice, we will compute one from a highly resolved numerical simulation). The discrete measured velocity fields $\boldsymbol{u}_h^n$ are the result of a subsampling operator, and therefore, they do not fulfill neither (1) nor a discretized version of it. Naturally, the same applies to $\boldsymbol{u}_m^n$, which includes additional random perturbations.

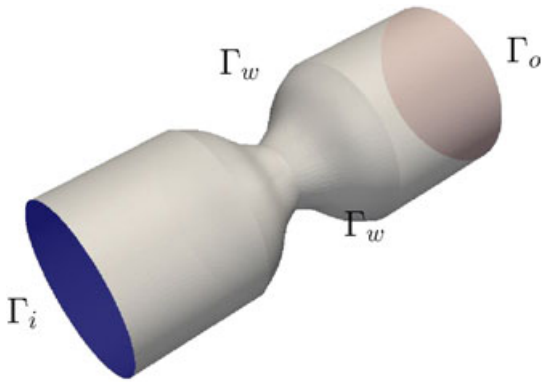

FIGURE 1 Stenosed geometry with 60% coarctation

3 | STATE OF THE ART OF ESTIMATION METHODS

In this section, we overview the mathematical formulations of the currently available methods to estimate relative pressure. We start with the *Poisson Pressure Estimator (PPE)*, which is the oldest and most popular. We continue with the *Stokes Estimator (STE)* and then with the *Work-Energy Relative Pressure (WERP) estimator*, both recently introduced. We remark that the later 2 approaches has been independently reported to have a superior performance than the PPE, but not have been yet compared with each other.

3.1 | The PPE

The PPE consists in solving a Poisson equation for the pressure, while the terms of the NSE containing the velocity are evaluated using the 3D-PCMRI measured velocities and therefore build a right-hand side.[20,24,25] When the PPE is solved by means of the finite element method,[25] the estimated relative pressure at time $t^{n+1/2} := (t^n + t^{n+1})/2$ can be found as the solution of the following weak formulation for the pressure: Find $p_{\text{ppe}}^{n+1/2} \in \mathcal{P}_{1,h}$ such that

$$\int_\Omega \nabla p_{\text{ppe}}^{n+1/2} \cdot \nabla q = -\frac{\rho}{\tau}\int_\Omega (\boldsymbol{u}_m^{n+1} - \boldsymbol{u}_m^n)\cdot \nabla q - \rho \int_\Omega (\boldsymbol{u}_m^{n+1/2}\cdot \nabla \boldsymbol{u}_m^{n+1/2})\cdot \nabla q \tag{3}$$

for all $q \in \mathcal{P}_{1,h}$, and $p_{\text{ppe}} = q = 0$ on Γ_o. Note that, since $\boldsymbol{u}_m^n \in [\mathcal{P}_{1,h}]^d$ does not possess enough regularity to compute its Laplacian, the viscous term in Equation 3 vanishes. Indeed it was reported in Lamata et al[27] that the viscous part of the pressure gradient in large vessels is negligible anyway.

Then the pressure drop at time $t^{n+1/2}$ between the outlet and the inlet is evaluated with Equation 2 using $p = p_{\text{ppe}}^{n+1/2}$. Note also that the midpoint time evaluation scheme allows a second-order approximation with respect to time and to reduce the noise variance of the measurements $\boldsymbol{u}_m^{n+1/2}$ by a factor of 2 with respect to the original variance of the measurements $\boldsymbol{u}_m^n$.

3.2 | The STE

The STE formulated in Švihlová et al[21] consists in perturbing the NSE with the Laplacian of an auxiliary divergence-free velocity field $\boldsymbol{w}$. This leads to a mixed problem for the pressure instead of a Poisson problem as in the PPE.

Defining $\mathcal{P}_{1,h}^b$ as the finite element space with linear piecewise polynomials with an additional bubble function at the centroid of the element, the STE is formulated as follows for the time step $t^{n+1/2}$ by the finite element solution of the following problem: Find $\boldsymbol{w} \in [\mathcal{P}_{1,h}^b]^d$ and $p_{ste}^{n+1/2} \in \mathcal{P}_{1,h}$, such that

$$\begin{aligned}\int_\Omega \nabla \boldsymbol{w} : \nabla \hat{\boldsymbol{w}} - \int_\Omega p_{ste}^{n+1/2}(\nabla\cdot\hat{\boldsymbol{w}}) + \int_\Omega (\nabla\cdot\boldsymbol{w})q = -\frac{\rho}{\tau}\int_\Omega (\boldsymbol{u}_m^{n+1} - \boldsymbol{u}_m^n)\cdot\hat{\boldsymbol{w}} \\ - \rho\int_\Omega (\boldsymbol{u}_m^{n+1/2}\cdot\nabla\boldsymbol{u}_m^{n+1/2})\cdot\hat{\boldsymbol{w}}\end{aligned} \tag{4}$$

for all $\hat{\boldsymbol{w}} \in [\mathcal{P}_{1,h}^b]^d$ and $q \in \mathcal{P}_{1,h}$, with $\boldsymbol{w} = \hat{\boldsymbol{w}} = \boldsymbol{0}$ on Γ. Then the pressure drop at time $t^{n+1/2}$ between the outlet and the inlet is evaluated with Formula (2) using $p = p_{\text{ste}}^{n+1/2}$. We remark that no additional information on the pressure field $p_{ste}^{n+1/2}$ is needed for ensuring solvability of Problem (4).[28] Notice also that, as for the PPE, the viscous term is neglected.

3.3 | The WERP

The starting point of the formulation of the WERP method introduced in Donati et al[22] is the classical energy relation of an incompressible Newtonian fluid, which can be obtained either by writing the conservation law for the energy density $\rho\boldsymbol{u}^2/2$ directly or multiplying (1) by $\boldsymbol{u}$ and integrating over Ω. This relation reads

$$\frac{\rho}{2}\int_\Omega \partial_t(|\boldsymbol{u}|^2) + \frac{\rho}{2}\int_\Gamma (\boldsymbol{u}\cdot\boldsymbol{n})|\boldsymbol{u}|^2 + \mu\int_\Omega |\nabla\boldsymbol{u}|^2 + \int_\Gamma p\,(\boldsymbol{u}\cdot\boldsymbol{n}) - \mu\int_\Gamma (\nabla\boldsymbol{u}\cdot\boldsymbol{n})\cdot\boldsymbol{u} = 0, \tag{5}$$

with $|\cdot|$ denoting the Euclidian norm.

The WERP is then formulated by assuming that (i) the measurements $\boldsymbol{u}_m^n$ satisfy relation (5), (ii) $\boldsymbol{u}_m^n \cdot \boldsymbol{n} \approx 0$ on Γ_w (ie, the vessel walls nearly do not move), (iii) the viscous forces on Γ are negligible, and (iv) the pressure is nearly constant on Γ_i and Γ_o. Doing so, the WERP pressure estimator at time $t^{n+1/2}$ is written as

$$\delta p_{werp}^{n+1/2}(\boldsymbol{u}_m^{n,n+1}) = \frac{-1}{\Lambda(\boldsymbol{u}_m^{n+1/2})}\left(E_{kin}(\boldsymbol{u}_m^{n+1}) - E_{kin}(\boldsymbol{u}_m^n) + E_{conv}(\boldsymbol{u}_m^{n+1/2}) + E_{visc}(\boldsymbol{u}_m^{n+1/2})\right) \tag{6}$$

with

$$E_{kin}(\boldsymbol{w}) = \frac{\rho}{2\tau}\int_\Omega |\boldsymbol{w}|^2 \tag{7}$$

$$E_{conv}(\boldsymbol{w}) = \frac{\rho}{2}\int_{\Gamma_i\cup\Gamma_o} (\boldsymbol{w}\cdot\boldsymbol{n})|\boldsymbol{w}|^2 \tag{8}$$

$$E_{visc}(\boldsymbol{w}) = \mu\int_\Omega |\boldsymbol{\nabla w}|^2 \tag{9}$$

$$\Lambda(\boldsymbol{w}) = \int_{\Gamma_i} \boldsymbol{w}\cdot\boldsymbol{n}. \tag{10}$$

Note that the superscript $n, n+1$ means that both velocity at the measured time steps n and $n+1$ are considered.

As it is well known from numerical analysis, the use of the midpoint scheme in (6) does not induce any perturbation compared with the time-continuous energy relation (5), independently on the time step τ.

We can see that this formulation may be unstable at small inflow/outflow because of the division by $\Lambda(\boldsymbol{u}_m^{n+1/2})$, ie, small imprecisions in this quantity lead to large imprecisions in the RPD. In other words, when the inflow is small, perturbations (eg, due to the presence of measurement noise) can induce large errors in $\Lambda(\boldsymbol{u}_m^{n+1/2})$ leading to an unphysical amplification of the estimated relative pressure. Fortunately, low-flow regimes are not relevant in clinical practice since only peak relative pressures are of interest. Another important issue is that the WERP induces systematic shifts in the pressure curve in the presence of noise, as we will see in the next section. Moreover, the WERP can only by construction estimate relative pressure in geometries with only one inflow and one outflow, because of the assumption $\boldsymbol{u}_m^n \cdot \boldsymbol{n} \approx 0$ on Γ_w needed to eliminate the pressure field on Γ_w out of the formulation.

4 | NEW ESTIMATION METHODS

In this section, we present new RPD estimation methods, inspired from the state-of-the-art approaches, and we will see later in the numerical examples that they can lead to improvements in the estimation results.

4.1 | The integrated STE

We propose to modify the STE method originally proposed in Švihlová et al[21] and formulated in Equation 4 by taking advantage of the regularity of the auxiliary velocity field and integrating the convective and viscous terms by parts. We will call this new methods the integrated STE (STEint).

The pressure drop estimated using the STEint for the time step $t^{n+1/2}$ corresponds to the finite element solution of the following problem: Find $\boldsymbol{w} \in [\mathcal{P}_{1,h}^b]^d$ and $p_{stei}^{n+1/2} \in \mathcal{P}_{1,h}$, such that

$$\begin{aligned}\int_\Omega \boldsymbol{\nabla w} : \boldsymbol{\nabla \hat{w}} - \int_\Omega p_{stei}^{n+1/2}(\boldsymbol{\nabla}\cdot\hat{\boldsymbol{w}}) + \int_\Omega (\boldsymbol{\nabla}\cdot\boldsymbol{w})q = &-\frac{\rho}{\tau}\int_\Omega (\boldsymbol{u}_m^{n+1} - \boldsymbol{u}_m^n)\cdot\hat{\boldsymbol{w}} \\ &+ \rho\int_\Omega (\boldsymbol{u}_m^{n+1/2}\cdot\boldsymbol{\nabla}\hat{\boldsymbol{w}})\cdot\boldsymbol{u}_m^{n+1/2} \\ &- \mu\int_\Omega \boldsymbol{\nabla u}_m^{n+1/2} : \boldsymbol{\nabla\hat{w}}\end{aligned} \tag{11}$$

for all $\hat{\boldsymbol{w}} \in [\mathcal{P}^b_{1,h}]^d$ and $q \in \mathcal{P}_{1,h}$, with $\boldsymbol{w} = \hat{\boldsymbol{w}} = \boldsymbol{0}$ on Γ. Notice that the boundary terms of the integration by parts do not appear since $\hat{\boldsymbol{w}} = \boldsymbol{0}$. Then the pressure drop at time $t^{n+1/2}$ between the outlet and the inlet is evaluated with Formula (2) using $p = p^{n+1/2}_{\text{stei}}$.

The advantage of reducing the derivative order of the measurements in the convective term will be noticeable in the robustness of the pressure estimation results when spatially subsampling the data. Unfortunately, this integration by parts is not straightforward for the PPE method because of the lack of enough regularity of $\boldsymbol{\nabla} q$ in Equation 3 when standard piecewise polynomial finite element spaces are used (like $\mathcal{P}_{1,h}$).

4.2 | The Darcy estimator

The STE approach perturbs the residual of the NSE with a divergence free term, which is in fact the Laplacian of a divergence-free vector. In principle, this is not necessarily the only option. If, instead of a Laplacian, a divergence free function is added directly, a Darcy, instead of a Stokes equation, appears. We propose then a new relative pressure estimator based on a discrete Darcy formulation, which we will denote the Darcy estimator (DAE).

It is well known from numerical analysis that, in this case, the Darcy equation requires a special type of finite elements spaces for ensuring correct solvability.[29,30] Let $\mathcal{RT}^k_h$ be the usual Raviart-Thomas finite element space of degree k. Then the DAE is formulated by the following finite element problem: Find $\boldsymbol{w} \in \mathcal{RT}^1_h$ and $p^{n+1/2}_{\text{dae}} \in \mathcal{P}_{1,h}$, such that

$$\begin{aligned}\int_\Omega \boldsymbol{w}\cdot\hat{\boldsymbol{w}} - \int_\Omega p^{n+1/2}_{\text{dae}}(\boldsymbol{\nabla}\cdot\hat{\boldsymbol{w}}) + \int_\Omega (\boldsymbol{\nabla}\cdot\boldsymbol{w})q = -\frac{\rho}{\tau}\int_\Omega (\boldsymbol{u}^{n+1}_m - \boldsymbol{u}^n_m)\cdot\hat{\boldsymbol{w}} \\ - \rho\int_\Omega (\boldsymbol{u}^{n+1/2}_m\cdot\boldsymbol{\nabla}\boldsymbol{u}^{n+1/2}_m)\cdot\hat{\boldsymbol{w}}\end{aligned} \tag{12}$$

for all $\hat{\boldsymbol{w}} \in \mathcal{RT}^1_h$ and $q \in \mathcal{P}_{1,h}$, with $\boldsymbol{w}\cdot\boldsymbol{n} = \hat{\boldsymbol{w}}\cdot\boldsymbol{n} = 0$ on Γ. This approach has not yet been reported, to the best of the authors knowledge. Note also that here, the integration by parts of the right-hand side, as by the STEint, is for regularity reasons not possible since $\hat{\boldsymbol{w}} \in \mathcal{H}_{\text{div}}(\Omega)$ and it can be easily shown that $\mathcal{H}_1(\Omega) \subset \mathcal{H}_{\text{div}}(\Omega)$.

4.3 | Integral momentum relative pressure estimator

Inspired by the WERP, in this section, we derive a new formulation for an integral relative pressure estimator based on a general class of test functions.

Assume that we have computed some specific function $\boldsymbol{v} \in \mathcal{H}_1(\Omega)$ satisfying

$$\boldsymbol{\nabla}\cdot\boldsymbol{v} \approx 0 \quad , \quad \boldsymbol{v}\cdot\boldsymbol{n} = 0 \text{ on } \Gamma_w. \tag{13}$$

If we multiply Equation 1_1 by $\boldsymbol{v}$ and we integrate over Ω

$$\underbrace{\rho\int_\Omega \partial_t\boldsymbol{u}\cdot\boldsymbol{v}}_{I_{kin}(\partial_t\boldsymbol{u})} + \underbrace{\rho\int_\Omega (\boldsymbol{u}\cdot\boldsymbol{\nabla}\boldsymbol{u})\cdot\boldsymbol{v}}_{I_{conv}(\boldsymbol{u})} + \underbrace{\int_\Omega \boldsymbol{\nabla}p\cdot\boldsymbol{v}}_{I_{pres}} \underbrace{-\mu\int_\Omega \Delta\boldsymbol{u}\cdot\boldsymbol{v}}_{I_{visc}(\boldsymbol{u})} = 0, \tag{14}$$

we obtain for each of the terms

$$I_{conv}(\boldsymbol{u}) = -\rho\int_\Omega (\boldsymbol{u}\cdot\boldsymbol{\nabla}\boldsymbol{v})\cdot\boldsymbol{u} + \rho\int_\Gamma (\boldsymbol{u}\cdot\boldsymbol{n})(\boldsymbol{u}\cdot\boldsymbol{v}) \tag{15}$$

$$I_{pres} = -\int_\Omega p(\boldsymbol{\nabla}\cdot\boldsymbol{v}) + \int_\Gamma p\ (\boldsymbol{v}\cdot\boldsymbol{n}) = \int_{\Gamma_i\cup\Gamma_o} p\ (\boldsymbol{v}\cdot\boldsymbol{n}) \tag{16}$$

$$I_{visc}(\boldsymbol{u}) = \mu\int_\Omega \boldsymbol{\nabla}\boldsymbol{u} : \boldsymbol{\nabla}\boldsymbol{v} - \mu\int_\Gamma (\boldsymbol{\nabla}\boldsymbol{u}\cdot\boldsymbol{n})\cdot\boldsymbol{v} \tag{17}$$

using standard integration by parts.

The integral momentum relative pressure estimator (IMRP) is then formulated by assuming that (i) the measurements $\boldsymbol{u}_m^n$ satisfy relation (14), and (ii) the pressure is nearly constant on Γ_i and Γ_o. Doing so, the IMRP estimator at time $t^{n+1/2}$ is formulated as

$$\delta p_{\text{imrp}}^{n+1/2}\left(\boldsymbol{u}_m^{n,n+1}\right) = -\frac{1}{\Lambda(\boldsymbol{v})}\left(I_{kin}\left(\frac{\boldsymbol{u}_m^{n+1}-\boldsymbol{u}_m^n}{\tau}\right) + I_{conv}\left(\boldsymbol{u}_m^{n+1/2}\right) + I_{visc}\left(\boldsymbol{u}_m^{n+1/2}\right)\right), \tag{18}$$

with $\Lambda(\cdot)$ the integral operator already defined in Equation 10.

Note that the requirements on the function in (13) serve only so that the pressure field vanishes (up to the relative pressure) in (16).

Notice also that the integral terms $I_{kin}, I_{conv}, I_{visc}$ are multiplied by $1/\Lambda(\boldsymbol{v})$ in the estimator formulation, which is independent of the measurements. This is an advantage compared to the WERP regarding the potential spurious amplifications for low flows mentioned above. Another advantage will be clear after the bias analysis. We also point out that we did not make any assumption on the velocity measurements on the boundary Γ_w, as it was done for the WERP. Hence, the IMRP allows a more flexible definition of the control volume where the pressure drop is computed with respect to the WERP.

We propose the test function $\boldsymbol{v}$ as the solution of the following Poiseuille flow, ie, a Stokes flow solution with unitary Neumann load on Γ_i. This is computed by the finite element solution of the following problem: Find $\boldsymbol{v} \in [\mathcal{P}_{1,h}^b]^d$ and $z \in \mathcal{P}_{1,h}$,

$$\int_\Omega \boldsymbol{\nabla v} : \boldsymbol{\nabla \psi} - \int_\Omega z\boldsymbol{\nabla}\cdot\boldsymbol{\psi} + \int_\Omega q\boldsymbol{\nabla}\cdot\boldsymbol{v} + \int_{\Gamma_i}\boldsymbol{\psi}\cdot\boldsymbol{n} = 0, \tag{19}$$

for all $\boldsymbol{\psi} \in [\mathcal{P}_{1,h}^b]^d$ and $q \in \mathcal{P}_{1,h}$, and with $\boldsymbol{v} = \boldsymbol{\psi} = \boldsymbol{0}$ on Γ_w. It is not necessary to introduce any coefficient in the viscous term in (19) since the IMRP estimator is independent of any constant linear scaling of the velocity field, see Equation 18. The same applies to the unitary Neumann load in (19). Note also that in the specific choice of this auxiliary function, since $\boldsymbol{v} = \boldsymbol{\psi} = \boldsymbol{0}$ on Γ_w all terms in that boundary in (15) to (17) vanish.

Remark 1. The final relative pressure estimation seems to not considerably depend on the order of the finite element space used for the test function in the numerical experiments. Differences between the different spaces can only be appreciated for coarse mesh spacing of the measurements, ie, larger than 3 mm. The same applies to the discretization of the STE, STEint, and DAE mixed problems.

5 | BIAS ANALYSIS

We remind the reader that we deal with additive random perturbations of the measured (subsampled) velocity. In this section, we detail how to compute the bias of the estimation methods introduced previously, what has not been done in any of the original works (ie, for PPE, STE, and WERP).

5.1 | Generalities

The computation of the bias b implies in practice to calculate the following quantity:

$$b = \mathbb{E}\left(\delta p^{n+1/2}\left(\boldsymbol{u}_h^{n,n+1} + \boldsymbol{\varepsilon}^{n,n+1}\right)\right) - \delta p^{n+1/2}\left(\boldsymbol{u}_h^{n,n+1}\right) \tag{20}$$

with $\mathbb{E}$ the usual expected value operator. Notice that it does not take into account the estimation errors due to the spatial or temporal subsampling. In simple words, bias is how much the mean of the estimators when including noise in the measurements differ from the estimator with noise-free measurements.

Since $\boldsymbol{\varepsilon}^n \in [\mathcal{P}_{1,h}]^d$ is a discrete noise field, we can write it (using the Einstein summation convention from now on) as $\varepsilon_i^n(\boldsymbol{x}) = N_j(\boldsymbol{x})e_{i,j}^n$, with $N_j(\boldsymbol{x})$ the finite element shape function for the jth degree of freedom of $\mathcal{P}_{1,h}$ and i denotes the spatial direction.

Remember also that the degrees-of-freedom $e^n_{i,j}$ are iid following a normal distribution $\mathcal{N}(0,\sigma^2)$ for all n,i,j. For any linear, differential operator with deterministic coefficients $\mathbb{D} : \mathcal{H}_1(\Omega) \to \mathcal{L}_2(\Omega)$, we have therefore the following identity:

$$\mathbb{E}\left(\int_\Omega \mathbb{D}(\boldsymbol{\varepsilon}^n_i)\right) = \int_\Omega \mathbb{E}\left(e^n_{i,j}\right)\mathbb{D}(N_j(\boldsymbol{x})) = 0 \tag{21}$$

5.2 | Pressure Poisson Estimator

To compute the bias (20) for the PPE method, we proceed as follows. Note that the bias function $b_{\text{ppe}} := \mathbb{E}(p^{n+1/2}_{\text{ppe}}(\boldsymbol{u}^{n,n+1}_m)) - p^{n+1/2}_{\text{ppe}}(\boldsymbol{u}^{n,n+1}_h)$ satisfies the problem: Find $b_{\text{ppe}} \in \mathcal{P}_{1,h}$ such that

$$\begin{aligned}\int_\Omega \boldsymbol{\nabla} b_{\text{ppe}} \cdot \boldsymbol{\nabla} q = \mathbb{E}\left(-\frac{\rho}{\tau}\int_\Omega \left(\boldsymbol{u}^{n+1}_m - \boldsymbol{u}^n_m\right)\cdot\boldsymbol{\nabla} q\right) + \frac{\rho}{\tau}\int_\Omega \left(\boldsymbol{u}^{n+1}_h - \boldsymbol{u}^n_h\right)\cdot\boldsymbol{\nabla} q \\ - \mathbb{E}\left(\rho\int_\Omega \left(\boldsymbol{u}^{n+1/2}_m \cdot \boldsymbol{\nabla}\boldsymbol{u}^{n+1/2}_m\right)\cdot\boldsymbol{\nabla} q\right) + \rho\int_\Omega \left(\boldsymbol{u}^{n+1/2}_h \cdot \boldsymbol{\nabla}\boldsymbol{u}^{n+1/2}_h\right)\cdot\boldsymbol{\nabla} q\end{aligned} \tag{22}$$

for all $q \in \mathcal{P}_{1,h}$, and $b_{\text{ppe}} = q = 0$ on Γ_o. Since $\boldsymbol{u}^n_m = \boldsymbol{u}^n_h + \boldsymbol{\varepsilon}^n$, the kinetic terms of the right-hand side of Problem (22) are zero because of Identity (21). For the convective terms, the only ones different from zero, since the expected value of the cross terms is zero because of Identity (21), are

$$\begin{aligned}\rho\int_\Omega \mathbb{E}\left((\boldsymbol{\varepsilon}^{n+1/2}\cdot\boldsymbol{\nabla}\boldsymbol{\varepsilon}^{n+1/2})\right)\cdot\boldsymbol{\nabla} q &= \rho\int_\Omega \mathbb{E}\left(\boldsymbol{\varepsilon}^{n+1/2}_k \partial_k \boldsymbol{\varepsilon}^{n+1/2}_i\right)\partial_i q \\ &= \rho\int_\Omega \mathbb{E}\left(N_j e^{n+1/2}_{k,j}\partial_k (N_\ell e^{n+1/2}_{i,\ell})\right)\partial_i q \\ &= \rho\int_\Omega \mathbb{E}\left(e^{n+1/2}_{k,j} e^{n+1/2}_{i,\ell}\right) N_j \partial_k N_\ell \partial_i q \\ &= \rho\int_\Omega \frac{\sigma^2}{2} N_j\partial_k N_j \partial_k q = \frac{\rho\sigma^2}{4}\int_\Omega \partial_k \sum_j (N_j)^2 \partial_k q \\ &= \frac{\rho\sigma^2}{4}\int_\Omega \boldsymbol{\nabla}\alpha\cdot\boldsymbol{\nabla} q\end{aligned}$$

with $\alpha = \sum_j (N_j)^2$ in $\mathcal{P}_{2,h}$. Therefore, we can compute the bias spatial distribution b_{ppe} by solving

$$\int_\Omega \boldsymbol{\nabla} b_{\text{ppe}}\cdot\boldsymbol{\nabla} q = -\frac{\rho\sigma^2}{4}\int_\Omega \boldsymbol{\nabla}\alpha\cdot\boldsymbol{\nabla} q. \tag{23}$$

with $b_{\text{ppe}} = q = 0$ on Γ_o. Finally, the bias for the relative pressure δp can be computed by evaluating Formula (2) with $p = b_{\text{ppe}}$.

We want to remark that this expression provides a closed form for the bias, depending only on known constants and the computational geometry itself. Therefore, it can be always evaluated a priori and, in the numerical examples, we will verify that turns to be negligible with respect to the relative pressure of interest. This will be also the case with the rest of the methods, except WERP.

5.3 | Stokes Estimator and DAE

Analogous to the PPE case, since they all share the same form for the right-hand side, the bias of STE and DAE can be computed by solving the following problems.

For the STE: Find $\boldsymbol{w} \in [\mathcal{P}^b_{1,h}]^d$ and $b_{\text{ste}} \in \mathcal{P}_{1,h}$, such that

$$\int_\Omega \boldsymbol{\nabla}\boldsymbol{w} : \boldsymbol{\nabla}\hat{\boldsymbol{w}} - \int_\Omega b_{\text{ste}}(\boldsymbol{\nabla}\cdot\hat{\boldsymbol{w}}) + \int_\Omega (\boldsymbol{\nabla}\cdot\boldsymbol{w})q = -\frac{\rho\sigma^2}{4}\int_\Omega \boldsymbol{\nabla}\alpha\cdot\hat{\boldsymbol{w}} \tag{24}$$

for all $\hat{\boldsymbol{w}} \in [\mathcal{P}^b_{1,h}]^d$ and $q \in \mathcal{P}_{1,h}$, with $\boldsymbol{w} = \hat{\boldsymbol{w}} = \boldsymbol{0}$ on Γ.

And now for the DAE, find $\boldsymbol{w} \in \mathcal{RT}_h^1$ and $b_{\text{dae}} \in \mathcal{P}_{1,h}$, such that

$$\int_\Omega \boldsymbol{w}\cdot\hat{\boldsymbol{w}} - \int_\Omega b_{\text{dae}}(\boldsymbol{\nabla}\cdot\hat{\boldsymbol{w}}) + \int_\Omega (\boldsymbol{\nabla}\cdot\boldsymbol{w})q = -\frac{\rho\sigma^2}{4}\int_\Omega \boldsymbol{\nabla}\alpha\cdot\hat{\boldsymbol{w}} \tag{25}$$

for all $\hat{\boldsymbol{w}} \in \mathcal{RT}_h^1$ and $q \in \mathcal{P}_{1,h}$, with $\boldsymbol{w}\cdot\boldsymbol{n} = \hat{\boldsymbol{w}}\cdot\boldsymbol{n} = 0$ on Γ.

5.4 | Integrated STE

Because of the integration by parts in the right-hand side, the STEint case has to be handled slightly different. Again, because of Identity (21), the kinetic and now also the viscous terms in the right-hand side of the bias equation vanish. The only nonzero term in the convective part has the form

$$\begin{aligned}\rho\int_\Omega \mathbb{E}\left((\boldsymbol{\varepsilon}^{n+1/2}\cdot\boldsymbol{\nabla}\hat{\boldsymbol{w}})\cdot\boldsymbol{\varepsilon}^{n+1/2}\right) &= \rho\int_\Omega \mathbb{E}\left(\boldsymbol{\varepsilon}_i^{n+1/2}\partial_i\hat{\boldsymbol{w}}_j\boldsymbol{\varepsilon}_j^{n+1/2}\right)\\ &= \rho\int_\Omega \mathbb{E}\left(e_{i,k}^{n+1/2}e_{j,\ell}^{n+1/2}\right)N_kN_\ell\partial_i\hat{\boldsymbol{w}}_j = \frac{\rho\sigma^2}{2}\int_\Omega \alpha\boldsymbol{\nabla}\cdot\hat{\boldsymbol{w}}.\end{aligned} \tag{26}$$

Therefore, for the STEint, the bias equation reads: Find $\boldsymbol{w} \in [\mathcal{P}_{1,h}^b]^d$ and $b_{\text{stei}} \in \mathcal{P}_{1,h}$, such that

$$\int_\Omega \boldsymbol{\nabla}\boldsymbol{w} : \boldsymbol{\nabla}\hat{\boldsymbol{w}} - \int_\Omega b_{\text{stei}}(\boldsymbol{\nabla}\cdot\hat{\boldsymbol{w}}) + \int_\Omega (\boldsymbol{\nabla}\cdot\boldsymbol{w})q = \frac{\rho\sigma^2}{2}\int_\Omega \alpha\boldsymbol{\nabla}\cdot\hat{\boldsymbol{w}} \tag{27}$$

for all $\hat{\boldsymbol{w}} \in [\mathcal{P}_{1,h}^b]^d$ and $q \in \mathcal{P}_{1,h}$, with $\boldsymbol{w} = \hat{\boldsymbol{w}} = \boldsymbol{0}$ on Γ.

5.5 | Integral momentum relative pressure

The bias of the IMRP can be directly defined as

$$b_{\text{irmp}} = \mathbb{E}\left(\delta p_{\text{imrp}}^{n+1/2}\left(\boldsymbol{u}_m^{n,n+1}\right)\right) - \delta p_{\text{imrp}}^{n+1/2}\left(\boldsymbol{u}_h^{n,n+1}\right).$$

It can be easily verified that because of Identity (21), the bias expression reduces to convective terms only:

$$\begin{aligned} b_{\text{irmp}} &= -\frac{1}{\Lambda(\boldsymbol{v})}\left(-\rho\int_\Omega \mathbb{E}\left(\boldsymbol{\varepsilon}_i^{n+1/2}\partial_j\boldsymbol{v}_i\boldsymbol{\varepsilon}_j^{n+1/2}\right) + \rho\int_\Gamma \mathbb{E}(\boldsymbol{\varepsilon}_i^{n+1/2}\boldsymbol{n}_i\boldsymbol{\varepsilon}_j^{n+1/2}\boldsymbol{v}_j)\right)\\ &= \frac{\rho\sigma^2}{2\Lambda(\boldsymbol{v})}\int_\Omega \alpha\boldsymbol{\nabla}\cdot\boldsymbol{v} - \frac{\rho}{\Lambda(\boldsymbol{v})}\int_\Gamma N_kN_\ell\boldsymbol{n}_i\boldsymbol{v}_j\mathbb{E}\left(e_{i,k}^{n+1/2}e_{j,\ell}^{n+1/2}\right)\\ &= \frac{\rho\sigma^2}{2\Lambda(\boldsymbol{v})}\int_\Omega \alpha\boldsymbol{\nabla}\cdot\boldsymbol{v} - \frac{\rho\sigma^2}{2\Lambda(\boldsymbol{v})}\int_\Gamma \alpha\boldsymbol{v}\cdot\boldsymbol{n}.\end{aligned}$$

5.6 | Work-energy relative pressure

We will now end the bias analysis with the WERP estimator. We will need for the analysis the following additional identities:

$$\mathbb{E}\left(\rho\int_\Omega |\boldsymbol{\varepsilon}^n|^2\right) = \sigma^2\text{tr}(\boldsymbol{M}_\Omega), \quad \mathbb{E}\left(\mu\int_\Omega |\boldsymbol{\nabla}\boldsymbol{\varepsilon}^{n+1/2}|^2\right) = \frac{\sigma^2}{2}\text{tr}(\boldsymbol{K}_\Omega), \tag{28}$$

with $\boldsymbol{M}_\Omega$ and $\boldsymbol{K}_\Omega$ the classical mass and stiffness finite element matrices for the Stokes problem in $\mathcal{P}_{1,h}$, respectively.

The goal is now to compute

$$b_{\text{werp}} = \mathbb{E}\left(\delta p_{\text{werp}}^{n+1/2}\left(\boldsymbol{u}_m^{n,n+1}\right)\right) - \delta p_{\text{werp}}^{n+1/2}\left(\boldsymbol{u}_h^{n,n+1}\right).$$

To perform such an analysis, we have to include the additional assumption that $\Lambda\left(\boldsymbol{u}_m^{n+1/2}\right) \approx \Lambda\left(\boldsymbol{u}_h^{n+1/2}\right)$, what is reasonable if we are interested in estimating the peak systolic RPD, which typically occurs simultaneous to the peak flow and therefore the velocity-to-noise ratio is best.

We proceed therefore as follows:

$$\mathbb{E}\left(\delta p_{werp}^{n+1/2}\left(\boldsymbol{u}_m^{n,n+1}\right)\right) \approx \frac{-1}{\Lambda\left(\boldsymbol{u}_m^{n+1/2}\right)}\mathbb{E}\left(E_{kin}\left(\boldsymbol{u}_m^{n+1}\right) - E_{kin}\left(\boldsymbol{u}_m^{n}\right) + E_{conv}\left(\boldsymbol{u}_m^{n+1/2}\right) + E_{visc}\left(\boldsymbol{u}_m^{n+1/2}\right)\right). \tag{29}$$

We now compute separately each term. First the kinetic part

$$\begin{aligned}\mathbb{E}\left(E_{kin}\left(\boldsymbol{u}_m^n\right)\right) &= \mathbb{E}\left(\frac{\rho}{2\tau}\int_\Omega |\boldsymbol{u}_h^n + \boldsymbol{\varepsilon}^n|^2\right)\\ &= \frac{\rho}{2\tau}\int_\Omega \mathbb{E}\left(|\boldsymbol{u}_h^n|^2 + 2\boldsymbol{u}_h^n\cdot\boldsymbol{\varepsilon}^n + |\boldsymbol{\varepsilon}^n|^2\right)\\ &= E_{kin}\left(\boldsymbol{u}_h^n\right) + \frac{\sigma^2}{2\tau}tr(\boldsymbol{M}_\Omega).\end{aligned}$$

Then the convective part can be reduced using Identity (21):

$$\begin{aligned}\mathbb{E}\left(E_{conv}(\boldsymbol{u}_m^n)\right) &= \frac{\rho}{2}\int_{\Gamma_i\cup\Gamma_o}\mathbb{E}\left(\left(\left(\boldsymbol{u}_h^n + \boldsymbol{\varepsilon}^n\right)\cdot\boldsymbol{n}\right)|\boldsymbol{u}_h^n + \boldsymbol{\varepsilon}^n|^2\right)\\ &= \frac{\rho}{2}\int_{\Gamma_i\cup\Gamma_o}\mathbb{E}\left(\left(\boldsymbol{u}_h^n\cdot\boldsymbol{n}\right)\left\{|\boldsymbol{u}_h^n|^2 + 2\boldsymbol{u}_h^n\cdot\boldsymbol{\varepsilon}^n + |\boldsymbol{\varepsilon}^n|^2\right\}\right.\\ &\quad\left. + \left(\boldsymbol{\varepsilon}^n\cdot\boldsymbol{n}\right)\left\{|\boldsymbol{u}_h^n|^2 + 2\boldsymbol{u}_h^n\cdot\boldsymbol{\varepsilon}^n + |\boldsymbol{\varepsilon}^n|^2\right\}\right)\\ &= E_{conv}\left(\boldsymbol{u}_h^n\right) + \frac{\rho}{2}\int_{\Gamma_i\cup\Gamma_o}\mathbb{E}\left(\left(\boldsymbol{u}_h^n\cdot\boldsymbol{n}\right)|\boldsymbol{\varepsilon}^n|^2 + 2(\boldsymbol{\varepsilon}^n\cdot\boldsymbol{n})\left(\boldsymbol{u}_h^n\cdot\boldsymbol{\varepsilon}^n\right)\right),\end{aligned}$$

where it can be easily shown that the very last (cubic) term in the second row vanishes because of the standard result that the cube of a normal variable has also zero expected value. Now, we continue using the fact that $\boldsymbol{\varepsilon}_i^n = N_j e_{i,j}^n$

$$\begin{aligned}\mathbb{E}\left(E_{conv}\left(\boldsymbol{u}_m^n\right)\right) &= E_{conv}\left(\boldsymbol{u}_h^n\right) + \frac{\rho}{2}\int_{\Gamma_i\cup\Gamma_o}\left(\boldsymbol{u}_h^n\cdot\boldsymbol{n}\right)\sum_i\mathbb{E}\left((N_j e_{i,j}^n)^2\right) + 2\mathbb{E}\left(\left(\boldsymbol{\varepsilon}^n\cdot\boldsymbol{n}\right)\left(\boldsymbol{u}_h^n\cdot\boldsymbol{\varepsilon}^n\right)\right)\\ &= E_{conv}(\boldsymbol{u}_h^n) + \frac{\rho}{2}\int_{\Gamma_i\cup\Gamma_o}\left(\boldsymbol{u}_h^n\cdot\boldsymbol{n}\right)(d\sigma^2)\alpha + 2\mathbb{E}\left(\left(N_k e_{i,k}^n\right)\left(N_\ell e_{j,\ell}^n\right)\right)\boldsymbol{n}_i\boldsymbol{u}_{h,j}^n\\ &= E_{conv}\left(\boldsymbol{u}_h^n\right) + \frac{\rho}{2}\int_{\Gamma_i\cup\Gamma_o}\left(\boldsymbol{u}_h^n\cdot\boldsymbol{n}\right)(d\sigma^2)\alpha + 2\sigma^2\alpha\boldsymbol{u}_h^n\cdot\boldsymbol{n}\\ &= E_{conv}\left(\boldsymbol{u}_h^n\right) + B_{conv}\left(\boldsymbol{u}_h^n,\sigma^2\right) \quad , \quad B_{conv}\left(\boldsymbol{u}_h^n,\sigma^2\right) = \frac{\rho\sigma^2(d+2)}{2}\int_{\Gamma_i\cup\Gamma_o}\left(\boldsymbol{u}_h^n\cdot\boldsymbol{n}\right)\alpha\end{aligned}$$

with d the spatial dimension (in our examples later $d = 3$). And at last, the viscous part

$$\begin{aligned}\mathbb{E}\left(E_{visc}\left(\boldsymbol{u}_m^{n+1/2}\right)\right) &= E_{visc}\left(\boldsymbol{u}_h^{n+1/2}\right) + \mu\int_\Omega 2\boldsymbol{\nabla}\boldsymbol{u}_h^{n+1/2} : \boldsymbol{\nabla}\boldsymbol{\varepsilon}^{n+1/2} + |\boldsymbol{\nabla}\boldsymbol{\varepsilon}^{n+1/2}|^2\\ &= E_{visc}\left(\boldsymbol{u}_h^{n+1/2}\right) + \frac{\sigma^2}{2}\mathrm{tr}(\boldsymbol{K}_\Omega).\end{aligned}$$

Now, we inserted the computed expected values into Equation 29, and we then obtain the following expression for the bias of the WERP estimator

$$b_{\mathrm{werp}} \approx \frac{-1}{\Lambda(\boldsymbol{u}_m^{n+1/2})}\left(\frac{1}{2}B_{conv}\left(\boldsymbol{u}_h^{n+1/2},\sigma^2\right) + \frac{\sigma^2}{2}\mathrm{tr}(\boldsymbol{K}_\Omega)\right) \quad . \tag{30}$$

Note that B_{conv} depends on both real (unknown) spatially subsampled velocity $\boldsymbol{u}_h^{n+1/2}$ and noise variance σ^2, while the second term of the bias depends on σ^2 and the geometry Ω only. However, we will show in the examples that this term is very small B_{conv} compared with the viscous part of the bias.

Remark 2. It is not straightforward to perform similar computations for the variance of the estimators. For the PPE, STE, STEint, and DAE, no expression or equation (to our knowledge) can be formulated. For the WERP and IMRP, even though the expressions for the pressure drop are explicit, in the variance, the expected value of products of integrals containing the noise is needed. This cannot be computed as before since these integrals are not iid.

6 | NUMERICAL EXAMPLES

In this section we present numerical results for the RPD estimation for the methods previously introduced.

6.1 | Forward simulations

The synthetic measurements are obtained from a Navier-Stokes simulation in a three-dimensional geometry representing a stenotic blood vessel, see Figure 1. The radii of inlet and outlet are 1 cm, and the stenosis has a radius of 0.4 cm, ie, 60% of coarctation. The physical parameters were chosen as $\mu = 0.035$ Poise and $\rho = 1.0$ gr/cm^3. An homogeneous Neumann load on Γ_o was imposed, while an homogeneous Dirichlet condition on Γ_w and the following Dirichlet condition on Γ_i are considered:

$$\boldsymbol{u} = 60(x^2 + z^2 - 1)\sin\left(\frac{5\pi}{2}t\right)\boldsymbol{n}, \text{ on } \Gamma_w, \tag{31}$$

where x, z are the coordinates of the plane perpendicular to the main flow direction (the vessel centerline lies on $x = z = 0$). These input data lead to a peak inflow rate and pressure drop of 94 cm^3/s and 21 mmHg, respectively. This pressure drop is typical from transitional coarctations from mild to severe and represents a typical threshold for clinical decisions.[31]

The numerical solution of the reference problem was performed using a monolithic velocity-pressure coupling. The space semidiscretization was performed with $\mathcal{P}^b_{1,h}/\mathcal{P}_{1,h}$ finite elements for the velocity and pressure, respectively, with a mesh spacing of $h = 0.06$ cm. A backward Euler scheme was used for the time semidiscretization with time-step of 0.002 second, with a semiimplicit treatment of the convective term, and including a Temam stabilization term to ensure Lyapunov stability of the solution in time.[32] At that spatial refinement level, no volume or backflow convective instabilities were observed, so no volume convective or backflow stabilization terms were included to not perturb the original equation, eg, SUPG[33] or backflow stabilization.[34-36]

6.2 | Synthetic measurements

Synthetic measurements (see Figure 2) were generated considering the following realistic perturbations of the data:

- First, the highly resolved reference solution was subsampled on grids with element spacing of 0.1, 0.15, 0.2, and 0.25 cm.
- Then it was subsampled in time at 0.02 seconds.

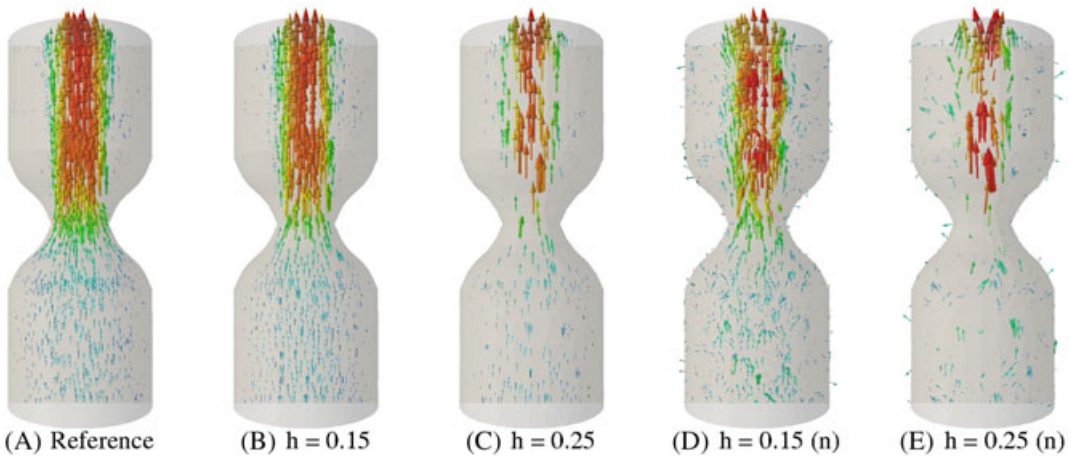

FIGURE 2 A, Reference simulated velocity field (with $h = 0.06$ cm and mini-elements). B-C, Spatially subsampled measurements at time $t = 0.25$ seconds (noise free). D-E, Spatially subsampled and noisy (n) measurements at time $t = 0.25$ seconds

- Finally, an additive Gaussian noise was added to the subsampled velocity at each mesh node and for each time. The standard deviation chosen as 10% of the peak velocity for all velocity components as it is usually done in clinical phase-contrast imaging adjusting the expected peak velocity (called *VENC* parameter).[9]

6.3 | Weighting functions for IMRP

We will use a Poiseuille flow as test functions $\boldsymbol{v}$ for the IMRP method, which it is shown in Figure 3.

We remark that this is not the only possible choice for $\boldsymbol{v}$. Alternatives may be Brinkman or Darcy flows. Nevertheless, in several numerical test that we performed, no advantage over a simple Poiseuille flow was established in the pressure gradient results. Specifically, the results of the Brinkman flow were dependent on the weighting of the mass term, possibly leading to deteriorated results if this weight was chosen either too large or too small. In the case of a Darcy flow, this is in fact a naive choice because of the lack of regularity of the solutions gradient, which is needed in the evaluation of the IMRP in Equation 18. A further option would be to include convective terms for $\boldsymbol{v}$, but this leads to considerably worse approximation results of the IMRP. Therefore, we do not present any results for these alternative test functions for the sake of clarity and conciseness.

6.4 | Bias of the estimators

As we remarked in Section 5, we can compute a priori the bias for all methods, which are shown in Table 1. Only in the case of the WERP, the bias coming from the convective term needs to be computed from the ground truth. However, we show that, for small mesh spacing, the bias of the WERP is dominated by the viscous part, which is again independent on the ground truth velocity field, see Equation 30.

For this example, the bias for the STE, STEint, and DAE is of the order of the machine precision. The bias of the PPE is also very small. The IMRP turns to give a negligible bias.

6.5 | Estimation results: noise-free measurements

We first study the sensitivity of the RPD estimation to spatial subsampling of the measurements, without any random noise. The results are shown in Figure 4, and the error convergence curves with respect to the data resolution h are shown in Figure 5. Note that the best methods turn out finally to be the IMRP and STEint, with the former giving a slightly better precision. They turn out to be more robust when subsampling the measurements compared with the state-of-the-art methods, ie, PPE, STE, and WERP. Note that the PPE, which is the oldest and the most spread approach, was consistently the worst method, in line with the findings of Švihlová et al[21,] and Donati et al.[22] We also remark that the temporal subsampling at this realistic level does not have a considerable impact on the estimation precision, compared with the space subsampling, and hence, only the time-subsampled results are shown for the sake of conciseness.

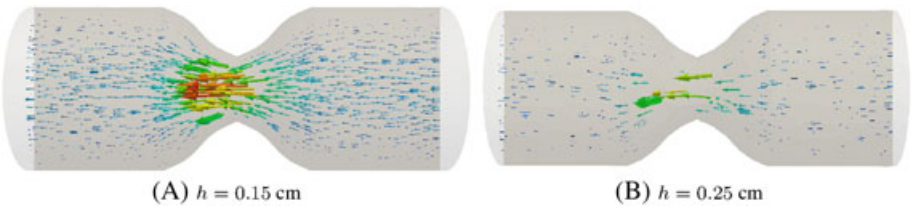

FIGURE 3 Poiseuille test functions for integral momentum relative pressure estimator for different spatial resolutions

TABLE 1 Computation of the estimators bias (mmHg) for 10% noise in the velocity

h [cm]	0.1	0.15	0.2	0.25
PPE	$5.7e-13$	$2.1e-13$	$1.4e-13$	$1.0e-13$
STE	$-1.6e-16$	$-1.0e-16$	$-1.6e-16$	$-1.6e-16$
STEint	$1.0e-17$	$8.6e-17$	$7.8e-17$	$-2.4e-17$
DAE	$3.3e-17$	$1.7e-16$	$7.0e-17$	$-9.6e-18$
WERP	2.3	0.9	0.6	0.5
WERP (visc)	2.3	1.0	0.3	1.1
IMRP	$4.2e-06$	$-5.1e-06$	$-7.9e-06$	$-4.1e-08$

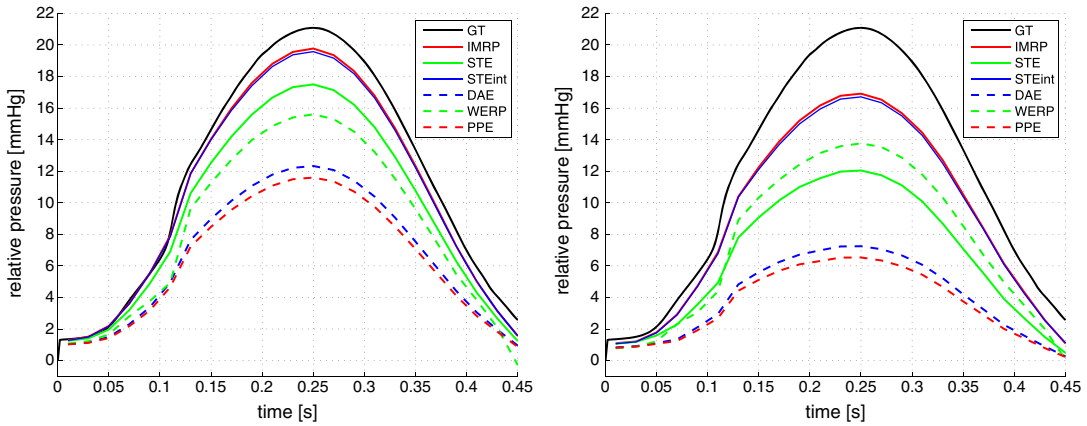

(A) $h = 0.15$ cm (B) $h = 0.25$ cm

FIGURE 4 Reference ground truth (GT) and noise-free relative pressure estimations for 2 different spatial subsampling resolutions including temporal subsampling of 0.02 second

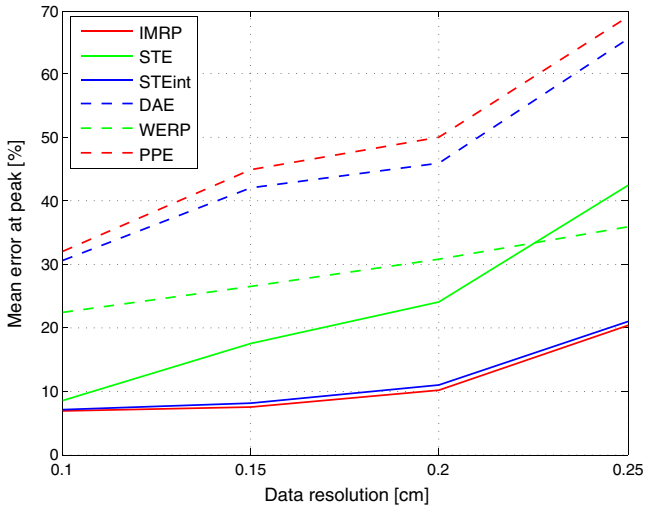

FIGURE 5 Error of estimation with respect to the ground truth at peak systole for noise-free but spatial subsampled measurements

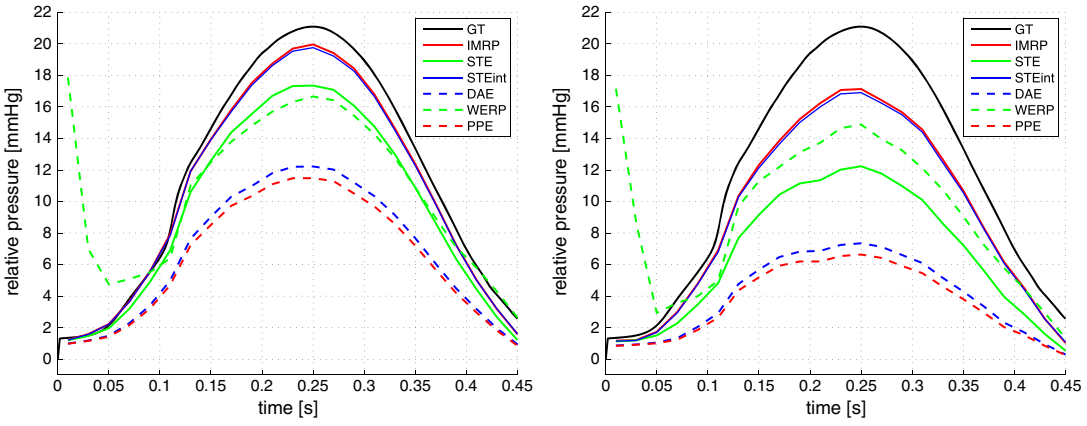

(A) $h = 0.15$ cm (B) $h = 0.25$ cm

FIGURE 6 Mean pressure estimations with noisy measurements

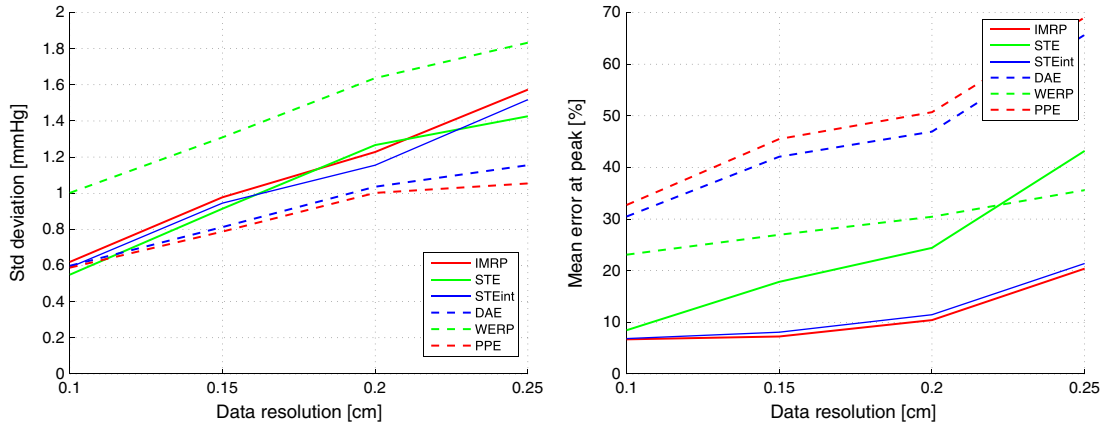

(A) Standard deviation (B) Mean error

FIGURE 7 Estimation results at peak systole with noisy measurements

6.6 | Estimation results: noisy measurements

Now, we summarize the results with noisy measurements, for which we consider independent 100 random realizations of the noise ϵ^n for each n. The standard deviations of the relative pressure estimation and the error of the mean with respect to the ground truth (both at peak systole) are presented in Figures 6 and 7. Note that both diminish with the spatial discretization size h for all methods. In addition, by comparing Figures 4 and 6, we verify that the bias is imperceptible, consistently with the values computed a priori in Table 1. Also consistent with Table 1, the only exception is the WERP.

As expected due to the "squaring" of the measurements, the method with highest variance is the WERP, while the methods delivering sharper standard deviations are PPE and DAE. However, the differences in standard deviations among all methods are around 1.0 mmHg, meaning around 2.0 mmHg for a 95% confidence interval.

In summary, these results confirm that, in this specific numerical example, the best performing methods (also when including noise and subsampling) are the IMRP and the STEint.

7 | DISCUSSION AND CONCLUSIONS

In this work, we reviewed, improved, analyzed (both theoretically and numerically), and compared old and recent approaches for estimating relatives pressures from 3D-PCMRI velocity data. The methods compared were the classical PPE,[25] the recently reported STE [21] and WERP,[22] and 3 new methods proposed in this work: the DAE, the STEint, and the IMRP.

The WERP method recently introduced in,[22] while being computationally the cheapest, it is more sensitive to noise, delivering biased estimations and larger variances than the other methods. Here it was confirmed, as in the original work, that the WERP performed better than the PPE. The bias of the WERP at higher data resolutions is controlled by the viscous term. However, in our specific numerical test, this term is anyway negligible with respect to the convective one, so it could be neglected from the WERP formulation, avoiding biasing.

We also performed computations for the STE method also recently introduced in Švihlová et al,[21] confirming that it performs better than the PPE. However, it also presented an error when the measurements are subsampled in space. We found out that just a simple integration by parts of the convective term considerably improves its precision in the presented example, and we called this new method STEint. This variant was not presented in the original article of STE.[21] In this context, we also investigated an alternative to the STE method based on the Darcy flow, which we called DAE, obtaining slightly better results than the PPE but worse than the rest of the approaches in terms of estimated mean RPD.

Finally, inspired from the integral approach introduced by the WERP, we proposed a new method based on an integral momentum balance weighted by a simple Poiseuille solution. This turns out to be the most accurate method together with the STEint, with a low sensitivity to spatial subsampling in current clinical ranges of voxel size used for 3D-PCMRI acquisitions.

Based on our numerical experiments, the methods of choice would be the IMRP and/or the STEint, both newly introduced in our contribution. While the STEint has the advantage of given a spatial distribution of the pressure (relative to

some point), the IMRP is computationally cheaper when the relative pressure needs to be computed at many time frames. This is since the mixed problem for $\boldsymbol{v}$ has to be solved only once, independent on the number of time frames, while for the STEint, the mixed problem has to be solved for each time that measurements are available. Future work will consist on further comparing and validating these approaches using real 3D-PCMRI data and catheter measurements.

ACKNOWLEDGMENTS

We sincerely thank discussions with Alfonso Caiazzo and Alexander Linke from WIAS Berlin about finite element discretizations, and with Sergio Uribe and Joaquín Mura from the Center for Biomedical Imaging of the Universidad Católica de Chile about Phase-Contrast MRI. D. Nordsletten acknowledges funding from BHF New Horizons program (NH/11/5/29058) and the Engineering and Physical Sciences Research Council (EP/N011554/1). The rest of the authors sincerely thank the Conicyt Basal Program PFB-03 for its support.

ORCID

Cristóbal Bertoglio http://orcid.org/0000-0001-5049-1707

REFERENCES

1. Jenkins NP, Ward C. Coarctation of the aorta: natural history and outcome after surgical treatment. *Qjm*. 1999;92(7):365-371.
2. Baumgartner H, Hung J, Bermejo J, et al. Echocardiographic assessment of valve stenosis: eae/ase recommendations for clinical practice. *J Am Soc Echocardiography*. 20091;22(1):1-23.
3. Cioffi G, Faggiano P, Vizzardi E, Tarantini L, Cramariuc D, Gerdts E, De Simone G. Prognostic effect of inappropriately high left ventricular mass in asymptomatic severe aortic stenosis. *Heart*. 2011;97(4):301-307.
4. Warnes CA, Williams RG, Bashore TM, et al. ACC/AHA 2008 guidelines for the management of adults with congenital heart disease. *J Am College Cardiol*. 2008;52(23):e143-e263.
5. Vahanian A, Alfieri O, Andreotti F, et al. Guidelines on the management of valvular heart disease (version 2012). *European Heart Journal*. 2012;33(19):2451-2496.
6. Haacke EM, Brown RW, Thompson MR, Venkatesan R, et al. *Magnetic Resonance Imaging: Physical Principles and Sequence Design*, Vol. 82. New York: Wiley-Liss; 1999.
7. Markl M, Frydrychowicz A, Kozerke S, Hope M, Wieben O. 4D flow MRI. *J Magn Reson Imag*. 2012;36(5):1015-1036.
8. Donati F, Myerson S, Bissel M, Smith N, Neubauer S, Monaghan M, Lamata NPD. Beyond bernoulli: improving the accuracy and precision of non-invasive estimation of peak pressure. *Circ Cardiovascular Imaging*. 2017;10:e005207.
9. Dyverfeldt P, Bissell M, Barker AJ, et al. 4D flow cardiovascular magnetic resonance consensus statement. *J Cardiovasc Magn Reson*. 2015;17(1):1-19.
10. DElia M, Perego M, Veneziani A. A variational data assimilation procedure for the incompressible navier-stokes equations in hemodynamics. *J Sci Comput*. 2012;52(2):340-359.
11. DElia M, Veneziani A. Uncertainty quantification for data assimilation in a steady incompressible navier-stokes problem. *ESAIM: Math Modell Numer Anal*. 2013;47(4):1037-1057.
12. Bertoglio C, Barber D, Gaddum N, et al. Identification of artery wall stiffness: in vitro validation and in vivo results of a data assimilation procedure applied to a 3d fluidstructure interaction model. *J Biomech*. 2014;47(5):1027-1034.
13. Goubergrits L, Riesenkampff E, Yevtushenko P, et al. Is MRI-based CFD able to improve clinical treatment of coarctations of aorta? *Ann Biomed Eng*. 2015;43(1):168-176.
14. Ismail M, Gee MW, Wall WA. *STACOM 2012, Nice, France*, chap. CFD Challenge: Hemodynamic Simulation of a Patient-Specific Aortic Coarctation Model with Adjoint-Based Calibrated Windkessel Elements. Berlin, Heidelberg: Springer Berlin Heidelberg; 2013;44-52.
15. Pant S, Fabrèges B, Gerbeau J-F., Vignon-Clementel IE. A methodological paradigm for patient-specific multi-scale CFD simulations: from clinical measurements to parameter estimates for individual analysis. *Int J Numer Methods Biomed Eng*. 2014;30(12):1614-1648.
16. Heys JJ, Manteuffel TA, McCormick SF, Milano M, Westerdale J, Belohlavek M. Weighted least-squares finite elements based on particle imaging velocimetry data. *J Comput Phys*. 2010;229(1):107-118.
17. Funamoto K, Hayase T, Saijo Y, Yambe T. Numerical experiment for ultrasonic-measurement-integrated simulation of three-dimensional unsteady blood flow. *Ann Biomed Eng*. 2008;36(8):13831397.
18. Bertoglio C, Chapelle D, Fernández M, Gerbeau J, Moireau P. State observers of a vascular fluidstructure interaction model through measurements in the solid. *Comput Methods Appl Mech Engrg*. 2013;256:149-168.
19. Moireau P, Bertoglio C, Xiao N, et al. Sequential identification of boundary support parameters in a fluid-structure vascular model using patient image data. *Biomech Model Mechanobiol*. 2013;12:475-496.
20. Ebbers T, Wigström L, Bolger AF, Engvall J, Karlsson M. Estimation of relative cardiovascular pressures using time-resolved three-dimensional phase contrast MRI. *Magn Reson Med*. 2001;45(5):872-879.

21. Švihlová H, Hron J, Málek J, Rajagopal K, Rajagopal K. Determination of pressure data from velocity data with a view toward its application in cardiovascular mechanics. Part 1. Theoretical considerations. *Int J Eng Sci*. 2016;105:108-127.
22. Donati F, Figueroa CA, Smith NP, Lamata P, Nordsletten DA. Non-invasive pressure difference estimation from PC-MRI using the work-energy equation. *Med Image Anal*. 2015;26(1):159-172.
23. Riesenkampff E, Fernandes JF, Meier S, et al. Pressure fields by flow-sensitive, 4d, velocity-encoded CMR in patients with aortic coarctation. *JACC: Cardiovasc Imaging*. 2014;7(9):920-926.
24. Ebbers T, Farnebäck G. Improving computation of cardiovascular relative pressure fields from velocity MRI. *J Magn Reson Imaging*. 2009;30(1):54-61.
25. Krittian SB, Lamata P, Michler C, et al. A finite-element approach to the direct computation of relative cardiovascular pressure from time-resolved MR velocity data. *Med Image Anal*. 2012;16(5):1029-1037.
26. Formaggia L, Quarteroni A, Veneziani A. *Cardiovascular Mathematics. Modeling and Simulation of the Circulatory System*, Vol. 1. Springer-Verlag Italia, Milano; 2009.
27. Lamata P, Pitcher A, Krittian S, et al. Aortic relative pressure components derived from four-dimensional flow cardiovascular magnetic resonance. *Magn Reson Med*. 2014;72(4):1162-1169.
28. Evans LC. *Partial Differential Equations: Second Edition*, Vol. 19. R.AMS. Graduate Series in Mathematics; Providence, Rhode Island; 2010.
29. Raviart P-A, Thomas J-M. A mixed finite element method for 2-nd order elliptic problems. *Mathematical Aspects of Finite Element Methods*. Springer; 1977:292-315.
30. Brezzi F, Douglas J Jr., Marini LD. Two families of mixed finite elements for second order elliptic problems. *Numerische Math*. 1985;47(2):217-235.
31. Warnes CA, Williams RG, Bashore TM, et al. ACC/AHA 2008 guidelines for the management of adults with congenital heart disease: a report of the American College of Cardiology/American Heart Association Task Force on practice guidelines (writing committee to develop guidelines on the management of adults with congenital heart disease). *Circulation*. 2008;118(1):714-833.
32. Temam R. Une méthode d'approximation de la solution des équations de navier-stokes. *Bull de la Soc Math de France*. 1968;96:115-152.
33. Brooks AN, Hughes TJ. Streamline upwind/Petrov-Galerkin formulations for convection dominated flows with particular emphasis on the incompressible Navier-Stokes equations. *Comput Methods Appl Mech Eng*. 1982;32(1):199-259.
34. Bertoglio C, Caiazzo A. A Stokes-residual backflow stabilization method applied to physiological flows. *J Comput Phys*. 2016;313:260-278.
35. Esmaily Moghadam M, Bazilevs Y, Hsia T-Y, Vignon-Clementel I, Marsden A of Congenital Hearts Alliance M. A comparison of outlet boundary treatments for prevention of backflow divergence with relevance to blood flow simulations. *Comput Mech*. 2011;48:277-291.
36. Kim H, Figueroa C, Hughes T, Jansen K, Taylor C. Augmented lagrangian method for constraining the shape of velocity profiles at outlet boundaries for three-dimensional finite element simulations of blood flow. *Comp Methods Appl Mech Engrg*. 2009;198(45):3551-3566.

How to cite this article: Bertoglio C, Nuñez R, Galarce F, Nordsletten D, Osses A. Relative pressure estimation from velocity measurements in blood flows: State-of-the-art and new approaches. *Int J Numer Meth Biomed Engng*. 2018;34:e2925. https://doi.org/10.1002/cnm.2925